Journal of Materials Chemistry A

PAPER

View Article Online
View Journal | View Issue

Cite this: J. Mater. Chem. A, 2017, 5, 18029

Exceptional catalytic activity of hollow structured $La_{0.6}Sr_{0.4}CoO_{3-\delta}$ perovskite spheres in aqueous media and aprotic Li–O_2 batteries†

Palanichamy Sennu,[a] Vanchiappan Aravindan,[b] Kee Suk Nahm[c] and Yun-Sung Lee*[a]

Received 15th May 2017
Accepted 30th July 2017

DOI: 10.1039/c7ta04189f

rsc.li/materials-a

Hollow structured $La_{0.6}Sr_{0.4}CoO_{3-\delta}$ (HS-LSC) perovskite spheres are synthesised *via* a template assisted approach and utilized as a bi-functional catalyst in both aqueous and non-aqueous media. Optimization of the calcination temperature has been performed to yield a single-phase HS-LSC. Rotating ring disk electrode measurements of HS-LSC in 0.1 M KOH exhibit two-fold higher (apex of limiting current is 4.974 mA cm^{-2}) oxygen evolution reaction (OER) capability than that of the commercial RuO_2 (1.84 mA cm^{-2}). The excellent oxygen reduction reaction (ORR) activity and durability up to 5400 s of HS-LSC also registered as comparable to those of Pt/C. The organic medium OER and ORR activities of the catalyst were explored from a Li–O_2 battery perspective. The HS-LSC catalyst based Li–O_2 battery delivered a deep discharge capacity of ~4895 mA h g^{-1} with high coulombic efficiency (~82%), and rate capability. Excellent cycling stability is also evidenced for a limited capacity of 500 mA h g^{-1}. Unprecedentedly, the favourable structural and morphological features facilitate O_2 transport, electrolyte immersion and ion diffusion processes promoting the catalytic reaction kinetics on the electrode.

Introduction

Over the last decade, research activities have accelerated to develop clean zero-carbon emission energy production from renewable resources, which effectively reduces both environmental pollution and suppresses the consumption of hydrocarbon fuel resources. Owing to the increased concern about the energy demands in large scale systems like electric vehicles and in grid storage, the lithium–oxygen (Li–O_2) battery is considered as the most efficient and eco-friendly power system compared to other renewable sources like traditional secondary batteries (Li-ion, Pb–acid, Ni–Cd & Ni–MH), fuel cells, water electrolysis and CO_2 to fuel conversion.[1–5] Furthermore, the high theoretical specific energy (~11.14 kW h kg^{-1} excluding O_2), light weight and lower cost are added advantages for such a fascinating system. The efficiency and durability of the cell is completely dependent on the fundamental surface electrochemistry of the electrodes and the working environment (aqueous, non-aqueous, hybrid and solid-state electrolytes).[2,6–10]

Bruce *et al.*[11] first demonstrated the enhanced reversible redox chemistry of a Li–O_2 battery in the presence of a MnO_2 catalyst in a carbonate based non-aqueous electrolyte. Later, McCloskey *et al.*[12] suggested the usage of nanostructured bifunctional catalysts which certainly minimizes the deep discharge overpotential and/or the enhancement of electron transportation in Li_2O_2. Therefore, utilization of high performance catalysts is very crucial for the development of the Li–O_2 system. Employing separate catalysts for oxygen evolution/reduction reactions (OER/ORR) in an O_2 electrode is a complex process, it requires complicated electrode design, and the practical reality is also not feasible. Hence, the usage of a bi-functional catalyst is highly desirable. Obviously, the OER/ORR activities in aqueous and organic media are entirely different, and hence the identification of suitable bifunctional catalysts is a hot topic of research in Li–O_2 batteries. In some exceptional cases, better catalytic activity is registered for both mediums.

The $ABO_{3-\delta}$ type of oxygen deficient $La_{1-x}Sr_xCoO_{3-\delta}$ perovskite exhibits mixed ionic/electronic conductivities and excellent O_2 exchange co-efficients, their superior bifunctional catalytic activities can replace the use of precious metals (Pt/RuO_2, IrO_2, *etc.*) in metal–air batteries and solid oxide fuel cell applications.[13–17] Suntivich *et al.*[18] reported that the OER activity of perovskites is directly correlated with the transition metal ion e_g orbital electron number or oxygen vacancy resulting from the B-site cation oxidation state. ORR and OER activities of different perovskite catalysts such as g-C_3N_4-$LaNiO_3$,[19] $LaMnO_3$,[20] and $CoSn(OH)_6$ (ref. 21) have been explored in both aqueous and

[a]Faculty of Applied Chemical Engineering, Chonnam National University, Gwang-ju 500-757, Republic of Korea. E-mail: leeys@chonnam.ac.kr

[b]Department of Chemistry, Indian Institute of Science Education and Research (IISER), Tirupati – 517507, India

[c]R&D Education Centre for Fuel Cell Materials & Systems, Chonbuk National University, Jeonju 561-756, Republic of Korea

† Electronic supplementary information (ESI) available. See DOI: 10.1039/c7ta04189f

non-aqueous media. Specifically, $La_{0.5}Sr_{0.5}CoO_{2.91}$ nanowires showed one order of magnitude higher specific capacity than is registered for its nanoparticle morphology in organic medium and similar enhancement is noted in aqueous medium too.[22] 3DOM $LaFeO_3$ nanostructured catalyst provides 14.3% higher specific capacity, high round trip efficiency and good rate capability over the Ketjen black-catalysed cell.[23] Thus, compared with low dimensional materials, the porous catalysts provide plenty of electrochemically active surface area, a conducting catalyst/gas diffusion layer, enhanced mass transfer and a mechanically stable buffer framework for the betterment of the Li–O_2 cell.[24,25]

In the present work, we synthesised hollow structured $La_{0.6}Sr_{0.4}CoO_{3-\delta}$ (HS-LSC) perovskite spheres through a template (carbon sphere) assisted approach using a refluxing method and adjusting the final calcination temperature. This was then employed as a bifunctional catalyst in a non-aqueous Li–O_2 battery during depth of discharge and capacity limited cycling (500 mA h g^{-1}). Besides organic solution, we also attempted to study the catalytic activity (OER and ORR) of HS-LSC in 0.1 M KOH solution as well. Apparently, rotating ring disk electrode (RRDE) measurements reveal that the HS-LSC displayed superior OER and ORR activity over commercial RuO_2 and Pt/C, respectively. Necessary structural and morphological properties are studied and described in detail.

Experimental section

Perovskite type $La_{0.6}Sr_{0.4}CoO_{3-\delta}$ hollow spheres were synthesised *via* a template assisted method. First, carbon nanosphere templates were derived from glucose solution using a hydrothermal process.[26] In a typical process, 80 ml of glucose solution (20 mmol) was transferred to a Teflon-lined autoclave and maintained at 180 °C for 10 h. The resultant black coloured product was washed several times with water and ethanol repeatedly, and dried at 60 °C overnight. Secondly, the stoichiometric amount (0.6 : 0.4 : 1 ratio) of $La(NO_3)_3\cdot 6H_2O$, $Sr(NO_3)_2$, $Co(NO_3)_2\cdot 6H_2O$ and urea (12 g) were dissolved in 90 ml of water, and a few minutes later 240 mg of dried carbon nanospheres were dispersed in the above solution. The resultant mixture was refluxed for 5 h at 120 °C, and the resultant brown coloured intermediate product was harvested and washed with ethanol. Finally, the dried products were calcined at different temperatures of 700, 800, 900 and 1000 °C for 5 h in O_2 atmosphere, and the corresponding porous hollow spheres were labelled as HS-LSC-7, HS-LSC-8, HS-LSC-9 and HS-LSC-10, respectively.

Physical characterization

A powder X-ray diffractometer (XRD, Rint 1000, Rigaku, Japan) equipped with CuKα radiation was used to study the structural properties. BET surface area measurements were conducted using a Micromeritics ASAP 2010 surface area analyzer. Surface morphological features of the samples were recorded using a field-emission scanning electron microscope (FE-SEM, S4700, Hitachi, Japan). X-ray photoelectron spectroscopy (XPS) was performed using a spectrometer (Multilab 2000, UK) with monochromatic Al Kα radiation ($h\nu = 1486.6$ eV).

Electrode preparation and electrochemical characterization

Rotating ring-disk electrode (RRDE). For the ORR and OER studies, the 3D Co-NC was mixed with carbon powder (Cabot Vulcan carbon XC-72) at a 30 : 70 wt% to ensure a sufficient electrical conductivity. Ten milligrams of the above mixture was dispersed ultrasonically in 150 μl of a diluted Nafion alcohol solution (5 wt%) in isopropyl alcohol (IPA). About 13.5 μl of the above suspension was drop-cast onto a 5.61 mm-diameter glassy carbon electrode [the area of the outer Pt ring is 0.2356 cm^2 (outer disc: 8.5 mm, inner disc: 6.5 mm)] as an RRDE electrode (Pine research instrumentation). The Co_3O_4-NS and a 20 wt% Pt/C electrode (Premetek Co.) were also studied for comparison. Cyclic voltammetry (CV) and linear sweep voltammetry (LSV) were recorded using a computerized potentiostatic instrument (model CHI700C). This three-electrode setup in a glass cell consisted of the RRDE as the working electrode, the Pt wire as the counter electrode, and Hg/HgO (1 M NaOH electrolyte) as a reference electrode immersed in O_2-saturated 0.1 M KOH as an electrolyte solution at ambient temperature conditions. The details of the reference electrode calibration are given in the ESI.† During CV measurements, the scan rate and the disk rotation speed are fixed at about 5 mV s^{-1} and 1600 rpm, respectively. Each analysis (ORR, OER and durability test) used the same mass loading and new electrodes (40 μg cm^{-2}).

Li–O_2 battery. For the formulation of the O_2 electrode, the catalyst and KB (1 : 2 ratio) were mixed with a Teflonized acetylene black (TAB-2) binder in isopropanol, formed into a pellet, and then pressed over a Ni mesh current collector. Furthermore, the electrodes were dried under vacuum at 100 °C for 12 h and subsequently employed as a cathode for the Li–O_2 battery. The catalytic performance of the catalyst was evaluated in Swagelok™-type Li–O_2 cells containing 1 M lithium bis(trifluoromethane)sulfonimide (LiTFSI) in a tetraethylene glycol dimethyl ether (TEGDME) electrolyte, and metallic lithium was used as the counter electrode. The CV traces were recorded within the range of 1.5–4.7 V *vs.* Li using a Won-A-Tech (WBCS 3000, Korea) battery tester. Galvanostatic charge/discharge cycling of the cells was recorded between 2–4.3 V *vs.* Li at different current densities (0.1–0.4 mA cm^{-2}) using a BTS 2004 (Japan) battery tester at room temperature.

Results and discussion

XRD patterns of the HS-LSC treated at different calcination temperatures are given in Fig. 1 (Fig. S1†). Accordingly, the collected patterns of HS-LSC can be indexed to the (110), (104), (024), (214), and (202) reflections of rhombohedral $La_{0.6}Sr_{0.4}CoO_{3-\delta}$ (ICDD 00-036-1393).[27] A phase pure structure is obtained only for the calcination at 1000 °C (HS-LSC-10). Below this temperature, secondary phases like $(La,Sr)_2CoO_4$ and La_2O_3 are observed at $2\theta = \sim 30$ and $\sim 37°$, respectively. Increasing the temperature from 700 to 1000 °C results in the disappearance of such secondary phases and leads to the formation of the pure

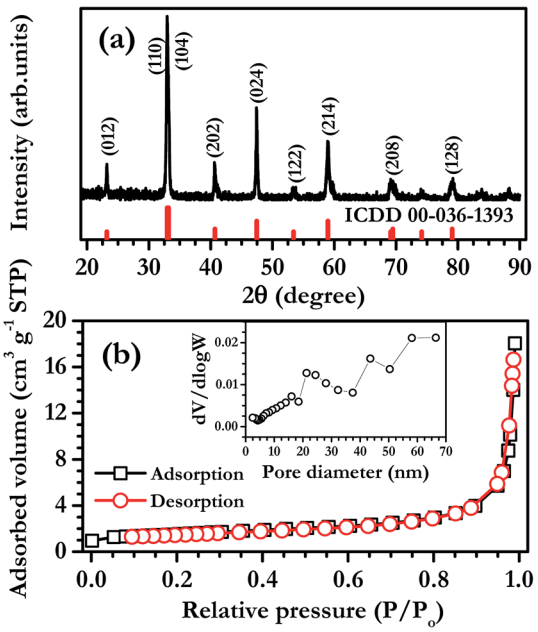

Fig. 1 (a) XRD and (b) BET specific surface area with pore size distribution (inset) of hollow sphere $La_{0.6}Sr_{0.4}CoO_{3-\delta}$ at 1000 °C (HS-LSC-10).

phase material.[28] Therefore, further studies are conducted on phase pure HS-LSC-10 only. Fig. 1b, shows the N_2 adsorption–desorption isotherms and pore size distribution of HS-LSC-10. Typically a type-IV N_2 sorption isotherm with H1 hysteresis loop relatively occurs at high pressure ($P/P_0 > 0.8$) indicating the mesoporous nature of the HS-LSC-10 prepared. Also, the average pore diameter of the HS-LSC-10 is estimated to be ~20 nm.

Surface morphology and microstructure of HS-LSCs were analysed by FE-SEM and HR-TEM, and presented in Fig. 2. Apparently, the SEM image of $La_{0.6}Sr_{0.4}CoO_{3-\delta}$ is of an open porous hollow sphere morphology which is obtained after the successful removal of the core carbon nanospheres. The non-uniform sized hollow sphere dimensions range from ~5 to 8 μm. The crystallinity and porosity of HS-LSC is increased with temperature (Fig. S2†). Fig. 2b shows the TEM image of HS-LSC-10 which is composed of nanoparticulates (~50 to 80 nm) with non-uniform porous morphologies (~40 nm). The HR-TEM picture reveals the highly crystalline nature of HS-LSC-10. The *d*-spacings are found to be ~0.266 and ~0.378 nm and correspond to the (110) and (012) planes of $La_{0.6}Sr_{0.4}CoO_{3-\delta}$, respectively. In addition, the selected area electron diffraction (SAED) pattern clearly shows a discontinued diffraction ring confirming a poly-crystalline nature (Fig. 2d). Furthermore, the observed rings can readily be indexed with the (312), (214), (024) and (202) planes of $La_{0.6}Sr_{0.4}CoO_{3-\delta}$ of rhombohedral phase and are consistent with the XRD results.

The investigation of the chemical composition and oxidation states of the elements present in HS-LSC-10 by XPS is shown in Fig. 3. Fig. 3a shows that the survey spectrum consists of different elements such as La, Sr, Co, O and C. Fig. 3b shows the Sr 3d spectrum de-convoluted and positioned at (131.3 ± 0.2 and 134.03 ± 0.2 eV) for $3d_{5/2}$ and (133 ± 0.2 and 135.3 ± 0.2 eV) for $3d_{3/2}$.[29] The lower and higher energy peaks arose from lattice and surface-bound Sr, respectively. Furthermore, the doublet separation (1.7 eV) and Sr binding energy in HS-LSC-10 are similar to those of Sr in SrO. Fig. 3c displays the de-convoluted La 3d peaks with binding energies of 833.6 and 837.2 eV which can be assigned to La $3d_{5/2}$ and La $3d_{3/2}$, respectively.[30] The small variations of the La $3d_{5/2}$ peak's binding energy and the spin–orbit splitting (~16.7 eV) undoubtedly confirms that the La ions are in a 3+ state and near the oxygen deficient sites. Fig. 3d shows that the core level Co 2p spectrum contains $2P_{3/2}$ and $2p_{1/2}$ peaks located at 780 ± 0.2 eV and 795 ± 0.2 eV, respectively. The spin–orbit doublet separation (15.1 eV) and

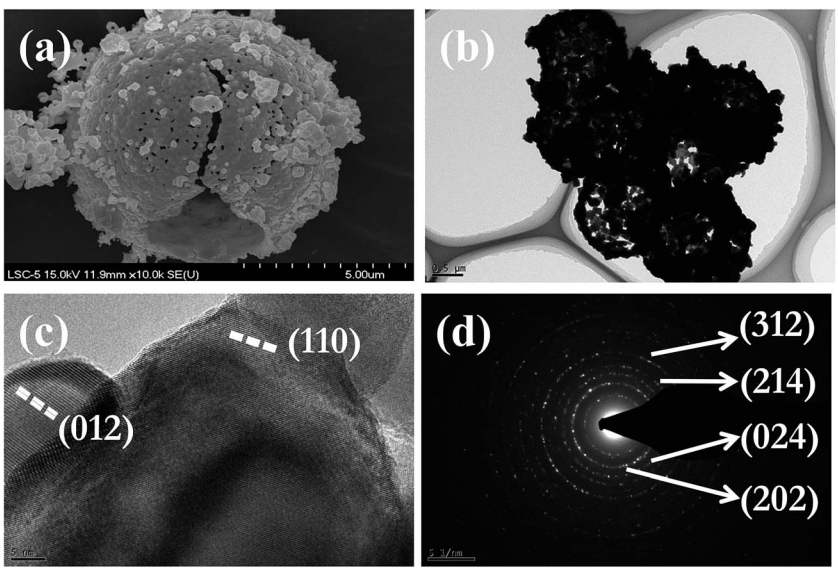

Fig. 2 (a) SEM, (b) TEM, (c) high resolution TEM and (d) selected area diffraction pattern of hollow sphere $La_{0.6}Sr_{0.4}CoO_{3-\delta}$ (HS-LSC-10).

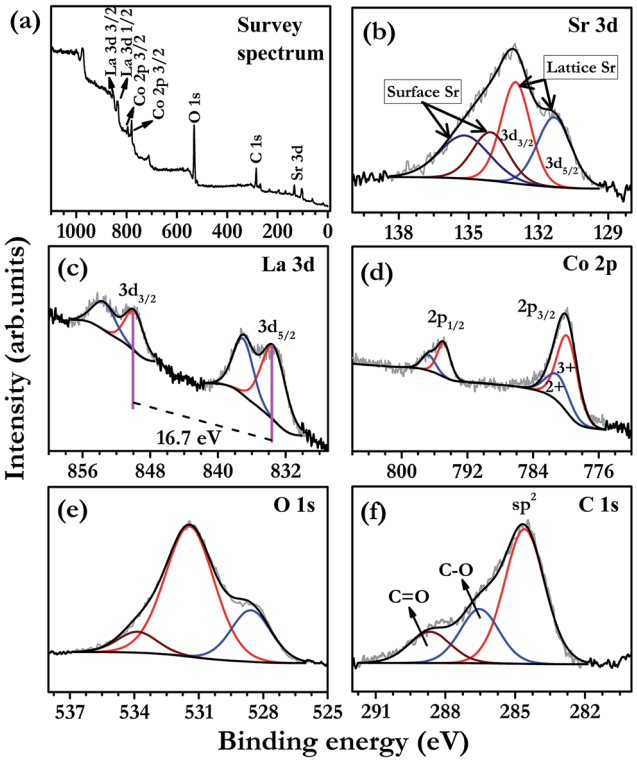

Fig. 3 X-ray photoelectron spectrum of hollow sphere $La_{0.6}Sr_{0.4}CoO_{3-\delta}$ (HS-LSC-10) (a) survey spectrum, (b) Sr 3d, (c) La 3d, (d) Co 2p, (e) O 1s and (f) C 1s.

the intensity ratio (0.5) are characteristic of Co^{2+} and Co^{3+} ions.[31,32] Fig. 3e and Fig. 3f confirm that the O 1s and C 1s peaks are located at ~531.5 ± 0.5 eV and ~284 ± 0.5 eV with different functionalities.[31]

Electrochemical studies

ORR and OER studies in aqueous medium. The electrochemical behaviour of the porous hollow sphere (HS-LSC-10) and nanoparticle LSC-10 (NP-LSC-10) catalysts has been studied in 0.1 M KOH aqueous electrolyte by the rotating ring-disk electrode (RRDE) technique, as shown in Fig. 4 and Table 1. The CV traces of the catalysts were recorded between −0.8 and 0.3 V *vs.* Hg/HgO at a scan rate of 5 mV s^{-1} and speed of 1600 rpm and are shown in Fig. S3.† A well-defined cathodic peak is observed at −0.21 and −0.229 V for the HS-LSC-10 and NP-LSC-10 catalysts in an O_2 saturated solution, respectively. The HS-LSC-10 peak shows a higher cathodic current (−0.217 mA cm^{-2}) with a greater positive shift than that of NP-LSC-10. In contrast, when the solution is saturated with N_2, a symmetric curve pattern was observed without any obvious peaks reflecting a double layer behaviour for HS-LSC-10. To gain more insight into the ORR activity of HS-LSC-10 and NP-LSC-10 from LSV, the catalytic activity of commercial Pt/C was also recorded between −0.8 and 0.3 V *vs.* Hg/HgO at a scan rate of 5 mV s^{-1} and speed of 1600 rpm for comparison and is shown in Fig. 4a. The onset potential of HS-LSC-10 is −0.154 V, which is shifted slightly towards a more positive potential than the NP-LSC-10 (−0.171 V). On the other hand, the potential of 0.109 V is noted for commercial Pt/C. The observed apex diffusion current for HS-LSC-10 is ~0.65 mA closer to that of Pt/C and slightly higher than that of the NP-LSC-10 catalyst. Notably, the excellent ORR catalytic performance results from the better electronic movements which facilitate efficient OH^- transportation to the HS-LSC-10 active sites.

Tafel slopes offer critical insight into the ORR analysis and are shown in Fig. 4b, all polarization curves are displayed at the low over potential regime between −0.4 to 0 V. Notably, there is a decreasing slope of the curve and an increase in the exchange current of HS-LSC-10 (88.7 mV dec^{-1}), close to that of commercial Pt/C, suggesting the beneficial electronic and geometric effects, and the exchange current is superior to that of NP-LSC-10 (107 mV dec^{-1}) as well. Fig. 4c shows that the increasing limiting diffusion current depends on the rotation speed and reveals the good ORR activity of the HS-LSC-10 catalyst. The OER activities of HS-LSC-10 and NP-LSC-10 were measured between 0.3 to 1 V *vs.* Hg/HgO at a scan rate of 5 mV s^{-1} and speed of 1600 rpm along with commercial RuO_2 and are shown in Fig. 4d. Anodic LSV measurements clearly indicate that, with a higher apex diffusion current (4.974 mA cm^{-2}) and much smaller overpotential of 0.769 V at the limiting diffusion current range of 1 mA cm^{-2}, the HS-LSC-10 displayed much better OER activity than the NP-LSC-10 and the state-of-the-art RuO_2 catalyst.

The ORR catalytic pathway and kinetic information for the HS-LSC-10, NP-LSC-10 and Pt/C catalysts were evaluated from the RRDE ring and disk currents shown in Fig. 5a. The ring current decreases significantly from NP-LSC-10 to HS-LSC-10 showing that the intermediate product formation (H_2O_2) was greatly decreased. The amount of peroxide species (OH_2^-) and number of electrons transferred (n) during ORR were calculated from the following eqn (1) and (2).[33,34]

$$\%\ \ OH_2^- = 200\ \frac{\frac{I_r}{N}}{I_d + \frac{I_r}{N}} \quad (1)$$

$$n = 4\frac{I_d}{I_d + \frac{I_r}{N}} \quad (2)$$

where, I_d and I_r are the disk current and ring current, respectively. N is the current collection efficiency in the RRDE (N = 0.37). The peroxide yield for HS-LSC-10 is 5–14% within the potential range of −0.8 to −0.2 V, which is lower than that of NP-LSC-10 (7–20%) as shown in Fig. 5b. In Fig. 5c, the number of electrons transferred for HS-LSC-10 is 3.71–3.90, which is higher than that of NP-LSC-10 (3.6–3.87). This result implies that oxygen reduction proceeds with a quasi-4 electron pathway in HS-LSC-10.

For practical applications, catalyst stability is one of the most important requirements. Thus, the durability of HS-LSC-10 and Pt/C was assessed by chronoamperometry at 0.6 V *vs.* Hg/HgO in O_2 saturated 0.1 M KOH with a speed of 1600 rpm over about 5400 s and is shown in Fig. 6. Apparently, no deviation from the current density of HS-LSC-10 is noted compared to Pt/C. This

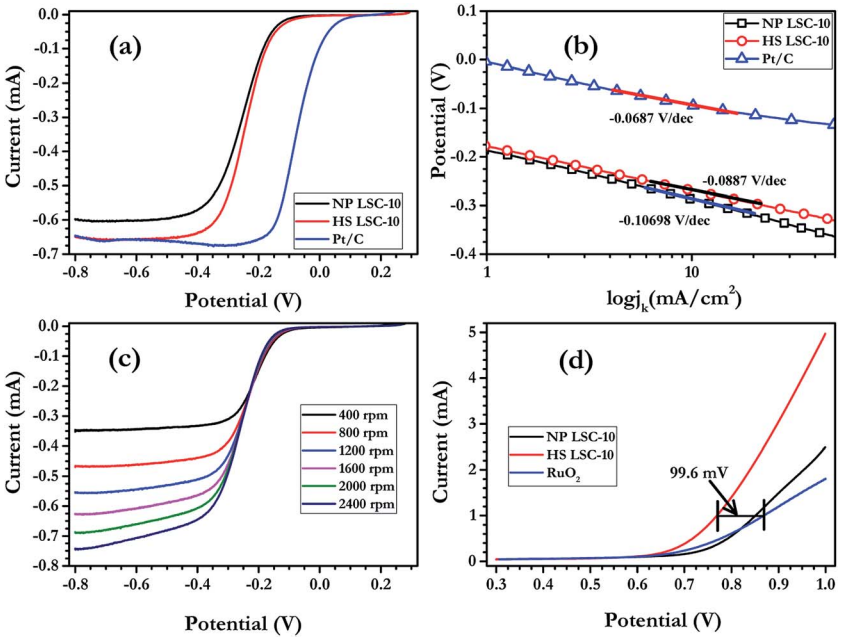

Fig. 4 Comparison (a) ORR and (b) OER linear sweep voltammetry at 1600 rpm speed, (c) ORR activity of the HS-LSC-10, and (d) Tafel plots of NP-LSC-10, HS-LSC-10 and Pt/C catalysts in O_2 saturated 0.1 M KOH electrolyte at a scan rate of 5 mV s^{-1}.

enhanced stability of the HS-LSC-10 catalyst reveals it to be useful as a potential catalyst for high performance applications like water splitting.

Li–O_2 battery. It is well known that the catalytic activity of a catalyst in aqueous and organic medium is entirely different, as is its reaction mechanism. Moreover, a successful catalyst in the aqueous media will not necessarily exhibit similar characteristics in an organic solution or *vice versa*. However, in some exceptional cases, better catalytic activity in both aqueous and organic media is reported, for example Co_3S_4 nanosheets,[7] g-C_3N_4-$LaNiO_3$ particles,[19] $LaMnO_3$ nanofibers,[20] *etc.* Further insight into the catalytic activity of HS-LSC-10 was examined in a Li–O_2 battery using the cyclic voltammetry method in the presence of an oxygen saturated 1 M LiTFSI in TEGDME electrolyte between 1.5 and 4.7 V *vs.* Li at a scan rate of 0.1 mV s^{-1} and is given in Fig. 7a. For comparison, NP-LSC-10 was also tested under the same conditions. A sharp oxygen reduction peak was observed at ~2.55 V *vs.* Li for both electrodes. However, the peak current and area underneath the curve for HS-LSC-10 is much higher than that of NP-LSC-10. This may be related to the porous hollow structure of HS-LSC-10 with its larger surface area that facilitates faster electron transfer through a network of connected catalytic sites and allows better oxygen diffusion compared to the NP-LSC-10 based cell. During the subsequent anodic scan, three distinguishable peaks with considerable peak currents were observed for the HS-LSC-10 electrode whereas the diminished peaks appearing below ~4.2 V *vs.* Li are featureless. However, a suppressed peak with large polarization is noted for the case of NP-LSC-10. The decomposition of discharge products on the HS-LSC-10 electrode at ~3.28 and ~3.57 V *vs.* Li is associated with the amorphous and crystalline form of Li_2O_2, respectively. In addition, the decomposition of the residual lithium carbonates (Li_2CO_3, HCO_2Li, CH_3CO_2Li, *etc.*) or electrolyte started at ~4.36 V *vs.* Li with a higher current response (0.3 mA) than NP-LSC-10 which exhibits a weak current (0.174 mA) and is shifted towards the higher potential of ~4.45 V *vs.* Li. Obviously, it is evident that the efficient catalytic activity with lower polarization of HS-LSC-10 is registered, which eventually enhances both energy output and round-trip efficiencies during reduction and oxidation processes compared to NP LSC-10 in the Li–O_2 battery assembly.[35–38]

Table 1 The cyclic voltammetry, ORR, OER and Tafel slope data for NP LSC-10, HS LSC-10 and commercial Pt/C, RuO_2 catalysts

	Cyclic voltammetry		ORR		OER		Tafel slope
Samples	Peak potential (V)	Peak current (mA cm^{-2})	Onset potential (V)	Apex current (mA cm^{-2})	Apex current (mA cm^{-2})	Onset potential (V)	Slope (V dec^{-1})
NP LSC-10	−0.229	0.163	−0.170	0.5977	2.49	0.851	−0.107
HS LSC-10	−0.21	0.217	−0.150	0.6487	4.97	0.769	−0.088
Pt/C	—	—	−1.090	0.6457	—		−0.068
RuO_2	—	—	—	—	1.84	0.868	—

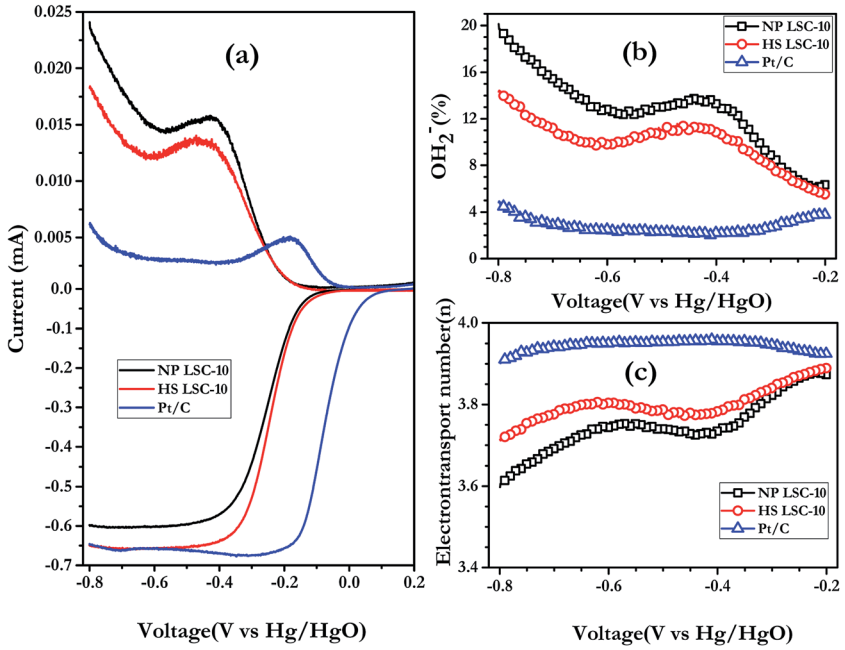

Fig. 5 RRDE measurements of (a) the ring and disk currents, (b) amount of peroxide formation of NP-LSC-10, HS-LSC-10 and Pt/C catalysts at speed of 1600 rpm in O_2 saturated 0.1 M KOH solution and (c) electron transference number.

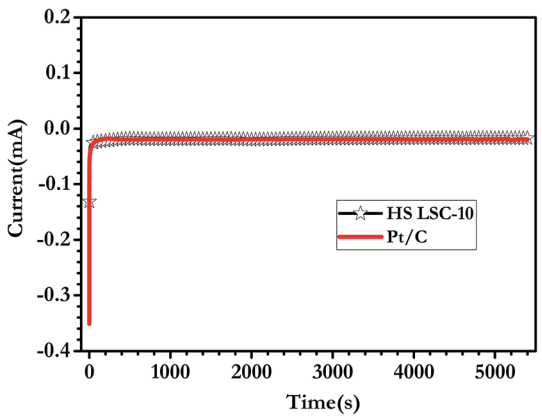

Fig. 6 ORR chronoamperometric response of HS-LSC-10 and Pt/C in O_2 saturated 0.1 M KOH electrolyte.

$$O_2^- + e^- + Li^+ \rightarrow LiO_2 \quad (3)$$

$$LiO_2 + e^- + Li^+ \rightarrow Li_2O_2 \quad (4)$$

$$Li_2O_2 \rightarrow Li_{2-x}O_2 \rightarrow 2 - xLi^+ + O_2 \quad (5)$$

Fig. 7b shows the first cycle depth charge–discharge curves of all HS-LSC catalysts conducted between 2 to 4.3 V *vs.* Li at a current density of 0.1 A g^{-1}. Here and in further studies, the operating voltage of the Li–O_2 battery is fixed from the above CV analysis result. Clearly, HS-LSC-10 delivered a very high first discharge capacity (~4895 mA h g^{-1}) and coulombic efficiency (~82%) compared to the other $La_{1-x}Sr_xCoO_{3-\delta}$ catalysts (ESI Table ST1†). The observed capacity is ~53% higher than that of

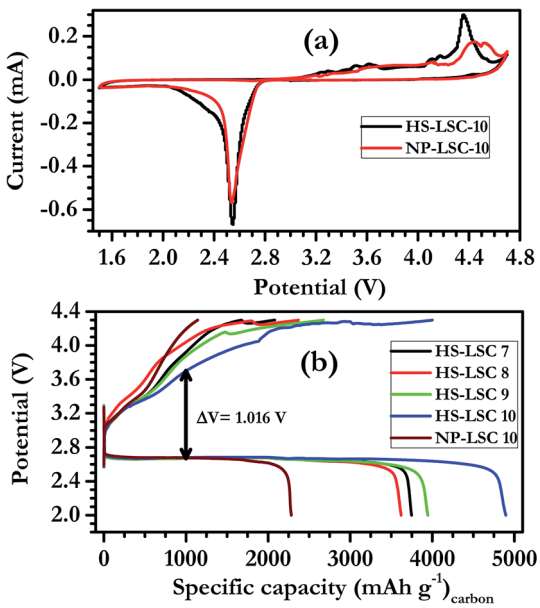

Fig. 7 (a) The cyclic voltammogram of Li–O_2 battery with HS LSC-10 and NP LSC-10 catalysts between 1.5 to 4.7 V at a sweep rate of 0.1 mV s^{-1}, (b) 1st cycle depth charge/discharge profile of HS LSC-7, HS LSC-8, HS LSC-9, HS LSC-10 and NP LSC-10 catalysts between 2 to 4.3 V at 100 mA g^{-1} current rate.

NP-LSC-10. It is worth mentioning that the increasing crystallinity of HS-LSC favours the improvement in coulombic efficiency with less over potential (validated at a specific capacity of 1000 mA h g^{-1}).

Fig. 8a shows the galvanostatic charge–discharge profile of the HS-LSC-10 electrode in the current density range from 0.1 to

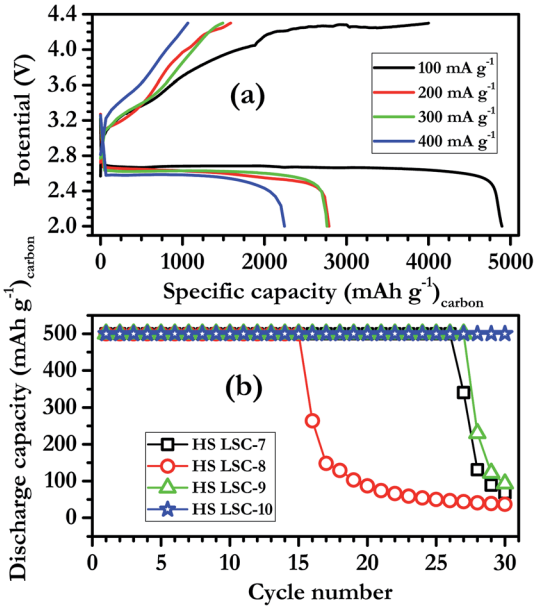

Fig. 8 (a) The rate performance of the Li–O_2 cell with HS LSC-10 catalyst at different currents ranging from 100 to 400 mA g^{-1}, (b) the cycling stability of Li–O_2 batteries in a limited capacity range with HS LSC-7, HS LSC-8, HS LSC-9 and HS LSC-10 catalysts at 100 m g^{-1} between 2 and 4.3 V.

0.4 A g^{-1} and the potential range of 2 to 4.3 V *vs.* Li. The discharge capacity and coulombic efficiency are decreased from 4895 to 1065 mA h g^{-1} and ~82 to 47%, respectively, when the current density is increased from 0.1 to 0.4 A g^{-1}. In addition, a small downturn in the discharge plateau at higher currents suggests a good rate capability. The cycleability of all the HS-LSC based Li–O_2 cells was investigated at a controlled/limited specific capacity of 500 mA h g^{-1} and a current density of 0.1 mA cm^{-2} as shown in Fig. 8b and Fig. S4.† The cycling performance and charge/discharge curves of the cell with the HS-LSC-10 electrode is much better than that of the other HS-LSC based cells. The overpotential (between charge and discharge) of the HS-LSC-7, HS-LSC-8 and HS-LSC-9 based electrodes was increased with increasing cycle number is another setback. The drastic polarization of the cell is followed by a serious cyclic degradation before 30 cycles.

Besides the excellent electro-catalytic activity in aqueous media, the porous electrode, facilitating both O_2 transport and Li^+ diffusion, and the hollow sphere allow more electrolyte immersion and collection of solid-state discharge products (Li_2O_2, Li_2CO_3). Moreover, the oxygen deficient crystal structure acts as an enhanced bifunctional active catalytic site, leading to an improvement in the round-trip efficiency and excellent long-term stability that is cost-effective compared with noble-metal catalysts.

Conclusion

Perovskite type porous hollow spheres of $La_{0.6}Sr_{0.4}CoO_{3-\delta}$ (HS-LSC) were synthesised through a template assisted procedure. The crystallinity, porosity and structural integrity were systematically investigated by XRD, SEM and TEM analysis. RRDE results of HS-LSC as a catalyst in 0.1 KOH show much improved bifunctional catalytic kinetics as compared with the particulate morphology and commercial Pt/C and RuO_2 catalysts. Furthermore, the non-aqueous Li–O_2 battery also showed a ~53% excess specific capacity with higher coulombic efficiency (~82%) than for the particulate morphology. More importantly, superior rate capabilities and a stable cycling performance under limited capacity cycling were demonstrated. The remarkable electrochemical performance of $La_{0.6}Sr_{0.4}CoO_{3-\delta}$ in both aqueous and organic media shows that this catalyst could be used as a cost effective potential candidate for fuel cells, water splitting and hybrid/non-hybrid metal–air batteries.

Acknowledgements

This work was supported by the Energy Efficiency & Resources Core Technology Program of the Korea Institute of Energy Technology Evaluation and Planning (KETEP), granted financial resources from the Ministry of Trade, Industry & Energy, Republic of Korea (20152010103470). VA thanks the financial support from the Science & Engineering Research Board (SERB), a statutory body of the Department of Science & Technology, Govt. of India through the Ramanujan Fellowship (SB/S2/RJN-088/2016).

References

1 L. Grande, E. Paillard, J. Hassoun, J.-B. Park, Y.-J. Lee, Y.-K. Sun, S. Passerini and B. Scrosati, The Lithium/Air Battery: Still an Emerging System or a Practical Reality?, *Adv. Mater.*, 2015, **27**, 784–800.
2 K. M. Abraham and Z. Jiang, A Polymer Electrolyte-Based Rechargeable Lithium/Oxygen Battery, *J. Electrochem. Soc.*, 1996, **143**, 1–5.
3 G. Girishkumar, B. McCloskey, A. C. Luntz, S. Swanson and W. Wilcke, Lithium–Air Battery: Promise and Challenges, *J. Phys. Chem. Lett.*, 2010, **1**, 2193–2203.
4 J. Christensen, P. Albertus, R. S. Sanchez-Carrera, T. Lohmann, B. Kozinsky, R. Liedtke, J. Ahmed and A. Kojic, A Critical Review of Li/Air Batteries, *J. Electrochem. Soc.*, 2011, **159**, R1–R30.
5 Y. Cui, Z. Wen and Y. Liu, A free-standing-type design for cathodes of rechargeable Li-O_2 batteries, *Energy Environ. Sci.*, 2011, **4**, 4727–4734.
6 M. Shao, Q. Chang, J.-P. Dodelet and R. Chenitz, Recent Advances in Electrocatalysts for Oxygen Reduction Reaction, *Chem. Rev.*, 2016, **116**, 3594–3657.
7 P. Sennu, M. Christy, V. Aravindan, Y.-G. Lee, K. S. Nahm and Y.-S. Lee, Two-Dimensional Mesoporous Cobalt Sulfide Nanosheets as a Superior Anode for a Li-Ion Battery and a Bifunctional Electrocatalyst for the Li–O_2 System, *Chem. Mater.*, 2015, **27**, 5726–5735.
8 M. Park, H. Sun, H. Lee, J. Lee and J. Cho, Lithium-Air Batteries: Survey on the Current Status and Perspectives

Towards Automotive Applications from a Battery Industry Standpoint, *Adv. Energy Mater.*, 2012, **2**, 780–800.

9 J. Lu, L. Li, J.-B. Park, Y.-K. Sun, F. Wu and K. Amine, Aprotic and Aqueous Li–O_2 Batteries, *Chem. Rev.*, 2014, **114**, 5611–5640.

10 F. S. Gittleson, R. C. Sekol, G. Doubek, M. Linardi and A. D. Taylor, Catalyst and electrolyte synergy in Li-O_2 batteries, *Phys. Chem. Chem. Phys.*, 2014, **16**, 3230–3237.

11 T. Ogasawara, A. Débart, M. Holzapfel, P. Novák and P. G. Bruce, Rechargeable Li_2O_2 Electrode for Lithium Batteries, *J. Am. Chem. Soc.*, 2006, **128**, 1390–1393.

12 B. D. McCloskey, R. Scheffler, A. Speidel, D. S. Bethune, R. M. Shelby and A. C. Luntz, On the Efficacy of Electrocatalysis in Nonaqueous Li–O_2 Batteries, *J. Am. Chem. Soc.*, 2011, **133**, 18038–18041.

13 S. Bie, Y. Zhu, J. Su, C. Jin, S. Liu, R. Yang and J. Wu, One-pot fabrication of yolk-shell structured $La_{0.9}Sr_{0.1}CoO_3$ perovskite microspheres with enhanced catalytic activities for oxygen reduction and evolution reactions, *J. Mater. Chem. A*, 2015, **3**, 22448–22453.

14 Z. Fu, X. Lin, T. Huang and A. Yu, Nano-sized $La_{0.8}Sr_{0.2}MnO_3$ as oxygen reduction catalyst in nonaqueous Li/O_2 batteries, *J. Solid State Electrochem.*, 2012, **16**, 1447–1452.

15 K.-N. Jung, J.-I. Lee, W. B. Im, S. Yoon, K.-H. Shin and J.-W. Lee, Promoting Li_2O_2 oxidation by an $La_{1.7}Ca_{0.3}Ni_{0.75}Cu_{0.25}O_4$ layered perovskite in lithium-oxygen batteries, *Chem. Commun.*, 2012, **48**, 9406–9408.

16 J. Scholz, M. Risch, K. A. Stoerzinger, G. Wartner, Y. Shao-Horn and C. Jooss, Rotating Ring–Disk Electrode Study of Oxygen Evolution at a Perovskite Surface: Correlating Activity to Manganese Concentration, *J. Phys. Chem.C*, 2016, **120**, 27746–27756.

17 S.-L. Zhang, H.-X. Yu, C.-X. Li, S. Y. Lai, C.-J. Li, G.-J. Yang, H.-B. Sun, T. Wei and M. Liu, Thermally sprayed high-performance porous metal-supported solid oxide fuel cells with nanostructured $La_{0.6}Sr_{0.4}Co_{0.2}Fe_{0.8}O_{3-\delta}$ cathodes, *J. Mater. Chem. A*, 2016, **4**, 7461–7468.

18 J. Suntivich, H. A. Gasteiger, N. Yabuuchi, H. Nakanishi, J. B. Goodenough and Y. Shao-Horn, Design principles for oxygen-reduction activity on perovskite oxide catalysts for fuel cells and metal–air batteries, *Nat. Chem.*, 2011, **3**, 546–550.

19 Y. Wu, T. Wang, Y. Zhang, S. Xin, X. He, D. Zhang and J. Shui, Electrocatalytic performances of g-C_3N_4-$LaNiO_3$ composite as bi-functional catalysts for lithium-oxygen batteries, *Sci. Rep.*, 2016, **6**, 24314.

20 K. R. Yoon, D. S. Kim, W.-H. Ryu, S. H. Song, D.-Y. Youn, J.-W. Jung, S. Jeon, Y. J. Park and I.-D. Kim, Tailored Combination of Low Dimensional Catalysts for Efficient Oxygen Reduction and Evolution in Li–O_2 Batteries, *ChemSusChem*, 2016, **9**, 2080–2088.

21 F. Song, K. Schenk and X. Hu, A nanoporous oxygen evolution catalyst synthesized by selective electrochemical etching of perovskite hydroxide $CoSn(OH)_6$ nanocubes, *Energy Environ. Sci.*, 2016, **9**, 473–477.

22 Y. Zhao, L. Xu, L. Mai, C. Han, Q. An, X. Xu, X. Liu and Q. Zhang, Hierarchical mesoporous perovskite $La_{0.5}Sr_{0.5}CoO_{2.91}$ nanowires with ultrahigh capacity for Li-air batteries, *Proc. Natl. Acad. Sci.*, 2012, **109**, 19569–19574.

23 J.-J. Xu, Z.-L. Wang, D. Xu, F.-Z. Meng and X.-B. Zhang, 3D ordered macroporous $LaFeO_3$ as efficient electrocatalyst for Li-O_2 batteries with enhanced rate capability and cyclic performance, *Energy Environ. Sci.*, 2014, **7**, 2213–2219.

24 D. Zhao, J.-L. Shui, L. R. Grabstanowicz, C. Chen, S. M. Commet, T. Xu, J. Lu and D.-J. Liu, Highly Efficient Non-Precious Metal Electrocatalysts Prepared from One-Pot Synthesized Zeolitic Imidazolate Frameworks, *Adv. Mater.*, 2014, **26**, 1093–1097.

25 Y. Yang, W. Yin, S. Wu, X. Yang, W. Xia, Y. Shen, Y. Huang, A. Cao and Q. Yuan, Perovskite-Type LaSrMnO Electrocatalyst with Uniform Porous Structure for an Efficient Li–O_2 Battery Cathode, *ACS Nano*, 2016, **10**, 1240–1248.

26 X. Sun and Y. Li, Colloidal Carbon Spheres and Their Core/Shell Structures with Noble-Metal Nanoparticles, *Angew. Chem., Int. Ed.*, 2004, **43**, 597–601.

27 M. Y. Oh, J. J. Lee, A. Zahoor, G. Gnana kumar and K. S. Nahm, Enhanced electrocatalytic activity of three-dimensionally-ordered macroporous $La_{0.6}Sr_{0.4}CoO_{3-\delta}$ perovskite oxide for Li-O_2 battery application, *RSC Adv.*, 2016, **6**, 32212–32219.

28 M. Kubicek, G. M. Rupp, S. Huber, A. Penn, A. K. Opitz, J. Bernardi, M. Stoger-Pollach, H. Hutter and J. Fleig, Cation diffusion in $La_{0.6}Sr_{0.4}CoO_{3-\delta}$ below 800 °C and its relevance for Sr segregation, *Phys. Chem. Chem. Phys.*, 2014, **16**, 2715–2726.

29 P. A. W. van der Heide, Systematic x-ray photoelectron spectroscopic study of $La_{1-x}Sr_x$-based perovskite-type oxides, *Surf. Interface Anal.*, 2002, **33**, 414–425.

30 E. Y. Konysheva, S. M. Francis, J. T. S. Irvine, A. Rolle and R.-N. Vannier, Redox behaviour in the $La_{0.6}Sr_{0.4}CoO_{3\pm\delta}$-$CeO_2$ system, *J. Mater. Chem.*, 2011, **21**, 15511–15520.

31 P. Sennu, H. S. Kim, J. Y. An, V. Aravindan and Y.-S. Lee, Synthesis of 2D/2D Structured Mesoporous Co_3O_4 Nanosheet/N-Doped Reduced Graphene Oxide Composites as a Highly Stable Negative Electrode for Lithium Battery Applications, *Chem.–Asian J.*, 2015, **10**, 1776–1783.

32 P. Sennu, H. S. Park, K. U. Park, V. Aravindan, K. S. Nahm and Y.-S. Lee, Formation of $NiCo_2O_4$ rods over Co_3O_4 nanosheets as efficient catalyst for Li–O_2 batteries and water splitting, *J. Catal.*, 2017, **349**, 175–182.

33 Y. Liang, Y. Li, H. Wang, J. Zhou, J. Wang, T. Regier and H. Dai, Co_3O_4 nanocrystals on graphene as a synergistic catalyst for oxygen reduction reaction, *Nat. Mater.*, 2011, **10**, 780–786.

34 P. Li, R. Ma, Y. Zhou, Y. Chen, Z. Zhou, G. Liu, Q. Liu, G. Peng, Z. Liang and J. Wang, *In situ* growth of spinel $CoFe_2O_4$ nanoparticles on rod-like ordered mesoporous carbon for bifunctional electrocatalysis of both oxygen reduction and oxygen evolution, *J. Mater. Chem. A*, 2015, **3**, 15598–15606.

35 K. P. C. Yao, M. Risch, S. Y. Sayed, Y.-L. Lee, J. R. Harding, A. Grimaud, N. Pour, Z. Xu, J. Zhou, A. Mansour, F. Barde and Y. Shao-Horn, Solid-state activation of Li_2O_2 oxidation

kinetics and implications for Li-O_2 batteries, *Energy Environ. Sci.*, 2015, **8**, 2417–2426.

36 C. O. Laoire, S. Mukerjee, K. M. Abraham, E. J. Plichta and M. A. Hendrickson, Influence of Nonaqueous Solvents on the Electrochemistry of Oxygen in the Rechargeable Lithium–Air Battery, *J. Phys. Chem. C*, 2010, **114**, 9178–9186.

37 J. Yi, X. Liu, S. Guo, K. Zhu, H. Xue and H. Zhou, Novel Stable Gel Polymer Electrolyte: Toward a High Safety and Long Life Li–Air Battery, *ACS Appl. Mater. Interfaces*, 2015, **7**, 23798–23804.

38 Y. Zhu, S. Liu, C. Jin, S. Bie, R. Yang and J. Wu, MnOx decorated CeO_2 nanorods as cathode catalyst for rechargeable lithium-air batteries, *J. Mater. Chem. A*, 2015, **3**, 13563–13567.